Research Article

Journal of Environmental Nanotechnology

Impact of Ferric Hydroxide Concentration on the Synthesis and Nitrate Removal Efficiency of gamma-Fe_2O_3Nanoparticles

Senniangiri Natarajan*, C. Dharanieswaran, A. Thomas Richard and S. Sudarsun
Department of Mechanical Engineering, Nandha Engineering College (Autonomous), Perundurai, Erode, TN, India
Received: 21.01.2026 Accepted: 04.03.2026 Published: 30.03.2026
*kannanselva1986@gmail.com

ABSTRACT

γ-Fe_2O_3 (maghemite or gamma iron oxide) nanoparticles were synthesized *via* an alcoholic sol–gel route using varying $Fe(OH)_3$ precursor concentrations (0.05–0.20 M) to systematically investigate the influence on nanoparticle yield, structural properties, and nitrate adsorption performance. Increasing the precursor concentration from 0.05 M to 0.15 M enhanced product yield while maintaining high surface area and optimal particle size. However, further increase to 0.20 M resulted in larger crystallite size and reduced surface area. Structural and morphological characteristics were confirmed by XRD, FTIR, BET, TGA/DSC, and FESEM analyses. Batch adsorption experiments at neutral pH demonstrated a maximum nitrate removal capacity of approximately 25 mg/g for nanoparticles synthesized at 0.15 M $Fe(OH)_3$. Adsorption kinetics followed the pseudo-second-order model, while equilibrium data were best described by the Langmuir isotherm, indicating monolayer adsorption behavior. The presence of competing anions slightly reduced nitrate removal efficiency, with sulfate exerting the most significant influence. The study establishes an optimal precursor concentration for high-yield synthesis of γ-Fe_2O_3 nanoparticles with enhanced nitrate adsorption capability, addressing the limited understanding of precursor concentration effects in alcoholic sol–gel systems.

Keywords: BET analysis; γ-Fe_2O_3 nanoparticles; Nitrate adsorption; Adsorption kinetics; Langmuir isotherm; Effect of $Fe(OH)_3$ concentration.

1. INTRODUCTION

Nitrate contamination in groundwater and drinking water is a growing environmental concern due to its contribution to eutrophication and associated health risks. Increasing agricultural runoff and industrial discharge have intensified nitrate accumulation in water bodies (Kumar and Basu, 2025). Although conventional treatment methods such as electrocoagulation and chemical precipitation have been explored for anion removal, these methods may generate sludge and require operational control (Wang *et al.* 2025). Adsorption has therefore emerged as a promising alternative due to its operational simplicity, cost-effectiveness, and adaptability for decentralized water treatment systems.

Metal hydroxides and metal oxides are widely investigated as adsorbents because of their abundant surface hydroxyl groups and strong affinity toward anionic contaminants. Ferric hydroxide-based materials have demonstrated effective removal of fluoride and other anions *via* ligand exchange and electrostatic interactions (Nyangi *et al.* 2021), (Demirkalp *et al.* 2016). Magnetic Fe_3O_4/$Fe(OH)_3$ composites and hybrid hydroxide systems have shown improved adsorption performance and stability (Hu *et al.* 2018), (Su *et al.* 2016). Modified $Fe(OH)_3$ systems, hybrid polymers, and surface-coated materials have also been applied for heavy metal and dye removal (Alagha *et al.* 2016), (Xu *et al.* 2025b). Electrocoagulation studies further confirm the effectiveness of *in situ* generated $Fe(OH)_3$ flocs for anion remediation (Sharma *et al.* 2024). Despite these developments, most reported investigations focus on fluoride, sulfate, heavy metals, or dyes rather than nitrate removal.

Iron oxide nanoparticles have attracted considerable attention for environmental remediation because of their chemical stability, environmental compatibility, and high surface reactivity. Fe_3O_4-based materials synthesized through sol–gel routes have been studied for photocatalytic, dielectric, and antimicrobial applications (El Nahrawy *et al.* 2020), (Song *et al.* 2024). Magnesite tailings were successfully used to remediate acid mine drainage which could remove >99% of most contaminants. Metal removal occurred through precipitation of metal hydroxides and chemisorption mechanisms (Masindi, 2016). Acid-treated *Pithecellobium dulce* seed pod powder effectively removed Reactive Red 195-A dye. Adsorption followed Temkin isotherm and pseudo-second-order kinetics, confirming spontaneous endothermic behavior (Baburao

et al. 2025). Polypyrrole was biosynthesized within *Aspergillus flavus* cell walls, forming a conductive and redox-active polymer. The PPy-AF2 culture showed superior electrochemical stability and catalytic potential (Girimurugan *et al.* 2024). Copper-doped cobalt oxide nanoparticles synthesized by microwave irradiation exhibited needle-like morphology. The nanostructures showed an indirect optical band gap of 4.52 eV with an average size of ~20 nm (Mayakannan *et al.* 2023). Amorphous aluminum oxalate enabled low-temperature synthesis of high-purity nano-AlN by carbothermal reduction. Compared to $Fe(OH)_3$, the precursor significantly reduced phase impurities and enhanced AlN formation efficiency (Tang *et al.* 2025).

Ultrafast Joule heating efficiently converted low-grade kaolin into high-purity zeolite 4A within seconds. The method outperformed conventional calcination by eliminating muscovite and quartz impurities (Fan *et al.* 2025). $Fe(OH)_3$-modified sugarcane bagasse biochar exhibited enhanced Cd^{2+} adsorption under optimized RSM conditions. Adsorption followed Langmuir isotherm and pseudo-second-order kinetics, indicating chemisorption behavior (Bakr *et al.* 2025). $Fe(OH)_3$ and $Zn(OH)_2$ nanoparticles demonstrated superior tetracycline removal compared to their oxide counterparts. Enhanced adsorption was attributed to higher surface activity and ionic potential of hydroxide forms (Zahra *et al.* 2025). *Speranskia tuberculata* extract achieved 97.29% hydrogen suppression from 7075-Al dust by adsorbing onto metal surfaces. Langmuir adsorption, surface passivation, and coordination bonding inhibited $Fe(OH)_3$ formation and hydrogen evolution (Xu *et al.* 2025a). $Fe(OH)_3$-reinforced bamboo-derived cellulose acetate films exhibited enhanced tensile strength and UV resistance. Uniform particle dispersion improved functional performance for sustainable packaging applications (Dong *et al.* 2024). Layered boehmite was synthesized in situ from high-alumina fly ash leachate, converting $Fe(OH)_3$ precursors into γ-AlOOH. The material showed high surface area and rapid Congo red adsorption (Wen *et al.* 2024). Agglomerated active seeds enhanced coarse $Fe(OH)_3$ precipitation from sodium aluminate solutions. Bayerite acted as a binder, while high temperature and alkalinity promoted agglomerate refinement (Shoppert *et al.* 2023).

In particular, the controlled use of $Fe(OH)_3$ precursor concentration as a synthesis-regulating parameter for tailoring γ-Fe_2O_3 nanoparticle characteristics toward enhanced nitrate removal has not been comprehensively investigated. Therefore, the present study systematically examines the effect of varying $Fe(OH)_3$ precursor concentration (0.05–0.20 M) in an alcoholic sol–gel route on the synthesis of gamma-Fe_2O_3 nanoparticles. The work evaluates structural transformation, crystallite growth, and surface area evolution, and correlates these properties with nitrate adsorption performance under neutral pH conditions. Adsorption kinetics and equilibrium behavior are analyzed using pseudo-first-order, pseudo-second-order, Freundlich, and Langmuir models to clarify the adsorption mechanism. By establishing the relationship between precursor concentration, nanoparticle characteristics, and nitrate removal efficiency, this study addresses the identified research gap and proposes an optimized synthesis strategy for gamma-Fe2O3 nanoparticles for water purification applications.

2. EXPERIMENTAL PROCEDURE

$Fe(OH)_3$ analytical grade), NH_4OH, 28 wt%, $NaNO_3$, Na_2SO_4, Na_2CO_3, NaCl, C_2H_5OH, 99.9%, HCl, and NaOH were used without further purification. Deionized water was used for all solution preparations.

2.1. Synthesis and Characterization of γ -Nano Iron Oxide Particles

To investigate the effect of precursor concentration on nanoparticle characteristics, controlled amounts of $Fe(OH)_3$ corresponding to nominal precursor concentrations of 0.05, 0.10, 0.15, and 0.20 mol per 500 mL reaction medium were dispersed in ethanol under continuous magnetic stirring for 4 hours. Since $Fe(OH)_3$ is sparingly soluble in ethanol, the system constitutes a suspension; therefore, concentrations are reported based on the molar amount of precursor introduced relative to total reaction volume. Ammonium hydroxide was added dropwise under vigorous stirring until the pH reached 7 ± 0.5. Under these conditions, partial hydrolysis and dehydration of $Fe(OH)_3$ occur, forming iron oxyhydroxide (FeOOH) nuclei through the following pathway as shown in equation (1):

$$Fe(OH)_3 \rightarrow FeOOH + H_2O \quad \ldots (1)$$

The suspension was aged for 24 hours to promote structural rearrangement and particle growth. The resulting precipitate was recovered by vacuum filtration, washed with ethanol and deionized water to remove residual ions, and dried at 100 °C for 3 hours. Calcination was performed at 450 °C for 80 min in a muffle furnace under air atmosphere to induce phase transformation of FeOOH into γ-Fe_2O_3 is represented in equation (2):

$$2FeOOH \rightarrow \gamma\text{-}Fe_2O_3 + H_2O \quad \ldots (2)$$

The calcined product was ground to obtain uniform nanopowder. This procedure represents a controlled precipitation–aging–calcination method rather than a classical alkoxide-based sol–gel route. The terminology has been revised accordingly for accuracy.

A similar synthesis technique was used for all four precursor concentrations (0.05–0.20 M) under uniform experimental conditions. The yield of γ-Fe_2O_3

nanoparticles was determined to be between 80% and 84%, aligning well with the theoretical yield anticipated for the current sol–gel–assisted precipitation method.

Thermogravimetric analysis (TGA) and differential scanning calorimetry (DSC) were conducted on the FeOOH precursor to examine its phase transition behavior, utilizing a LABSYS EVO under nitrogen environment up to 900 °C at a heating rate of 10 °C min^{-1}. The TGA/DSC profiles were generated by graphing relative weight change (%) against temperature. Phase identification and crystallographic verification of FeOOH and γ-Fe_2O_3 nanoparticles were conducted by X-ray diffraction (XRD) analysis utilizing a Bruker (Model: D8 advance) with Cu Kα radiation (λ = 1.5406 Å), operating at 40 kV and 40 mA within a 2θ range of 10°–90° at a scan rate of 2° min^{-1}. The surface appearance and particle distribution of the gamma-Fe_2O_3 nanoparticles were analyzed using a field emission scanning electron microscope (Zeiss, Gemini) operated at an accelerating voltage of 10–15 kV. Characteristic functional groups and bonding environments were investigated using Fourier transform infrared spectroscopy (FTIR) with a Shimadzu IRSpirit-X across the range 4000–400 cm^{-1}. The specific surface area of the γ-Fe_2O_3 nanoparticles was ascertained by the Brunauer–Emmett–Teller (BET) method utilizing nitrogen adsorption, using an Anton Paar Autorun IQ surface area analyzer. Samples were degassed at 150 °C for 4 hours prior to measurement.

2.2 Batch Adsorption and Nitrate Evaluation

A research on nitrate removal was conducted at room temperature utilizing a batch test. A solution of 1000 mg/L nitrate was prepared by dissolving 2.322 g sodium nitrate at 1 L of deionized water. Solutions of various concentrations were prepared through serial dilutions of stock solution. Subsequently, batch adsorption experiments were conducted in 150 mL conical flasks containing 50 mL nitrate solution and a fixed adsorbent dosage (50 mg). The pH was adjusted to 7 ± 0.2 using dilute NaOH. The flasks were agitated at 100 rpm at room temperature (30 ± 2 °C).

$$q_e = (C_0 - C_e)V/m \quad \ldots (3)$$

q_e represents nitrate adsorption (mg/g), C_0 denotes total nitrate concentration (mg/L) of working solution, C_e denotes residual nitrate (mg/L) remaining post-batch adsorption, V represents volume of the solution, and m denotes mass of adsorbent utilized at batch operation.

To evaluate selectivity under realistic water chemistry conditions, competitive adsorption experiments were conducted by adding 20 mg/L of SO_4^{2-}, CO_3^{2-}, Cl^-, or NO_3^- (background) individually to nitrate-containing solutions. These anions were selected because they commonly coexist in natural groundwater and compete for surface hydroxyl adsorption sites *via* electrostatic interaction or inner-sphere complexation.

3. RESULTS AND DISCUSSION

3.1. Synthesis and Characterization

Iron(III) hydroxide is likely to convert into boehmite (FeOOH) gel following a hydrolysis reaction in presence of NH_4OH. During the aging stage, $Fe(OH)_3$ undergoes partial dehydration and structural rearrangement to form FeOOH. The XRD pattern of the dried precursor (100 °C, 1 hour) corresponding to the 0.05 mol $Fe(OH)_3$ sample (Figure 1a) exhibits broad and low-intensity reflections, indicating poor crystallinity of the FeOOH phase. Similar diffraction features were observed for precursor samples prepared with 0.10, 0.15, and 0.20 mol $Fe(OH)_3$, confirming comparable precursor phase formation prior to calcination. Upon calcination at 450 °C, FeOOH undergoes thermal dehydration to form gamma-Fe_2O_3. The XRD patterns of the calcined samples (Figure 1b–c) clearly confirm the formation of crystalline gamma-Fe_2O_3 with a cubic spinel structure. The characteristic diffraction peaks observed at 2θ ≈ 30.2°, 35.6°, 43.3°, 53.7°, 57.3°, and 62.9° are indexed to the (220), (311), (400), (422), (511), and (440) crystallographic planes, respectively, in good agreement with standard JCPDS card No. 39-1346 for gamma-Fe_2O_3. No additional peaks corresponding to α-Fe_2O_3 (hematite) or other secondary phases were detected within the instrumental detection limits, confirming phase purity.

With increasing $Fe(OH)_3$ precursor concentration, the diffraction peaks become sharper and more intense, indicating improved crystallinity and grain growth. A slight shift in the (440) reflection was observed for the 0.20 mol sample, with the corresponding d-spacing increasing from approximately 1.401 Å (0.05–0.15 mol samples) to 1.408 Å for the 0.20 mol sample. This minor variation may be attributed to lattice strain or crystal growth effects associated with higher precursor loading. Increased peak sharpness and reduced peak broadening at higher concentration further indicate crystallite enlargement. According to previous demonstrates, XRD patterns confirmed the crystalline spinel structure of gamma-Fe_2O_3 (maghemite) in the silica nanocomposite with well-defined characteristic peaks. Scherrer analysis revealed an average maghemite crystallite size of approximately 11 nm (Tural *et al.* 2011).

The average crystallite size of gamma-Fe_2O_3 nanoparticles was estimated using the Scherrer equation:

$$D = K\lambda/\beta\cos\theta \quad \ldots (4),$$

where K = 0.9 is the shape factor (assuming spherical crystallites), λ = 1.5406 Å (Cu Kα radiation), β

is the full width at half maximum (FWHM) of the (311) diffraction peak expressed in radians and corrected for instrumental broadening, and θ is the corresponding Bragg angle. The (311) reflection was selected for size estimation due to its highest intensity and reliability. The calculated crystallite sizes ranged from approximately 28–32 nm for the 0.05–0.15 mol samples, whereas the 0.20 mol sample exhibited a larger average crystallite size of approximately 38–42 nm. These results demonstrate that increasing precursor concentration beyond 0.15 mol promotes crystallite growth, leading to increased crystal size while maintaining the cubic spinel gamma-Fe_2O_3 phase stability. SEM images depicted at Figure 2 illustrate that the nanoparticles are predominantly spherical and exhibit agglomeration.

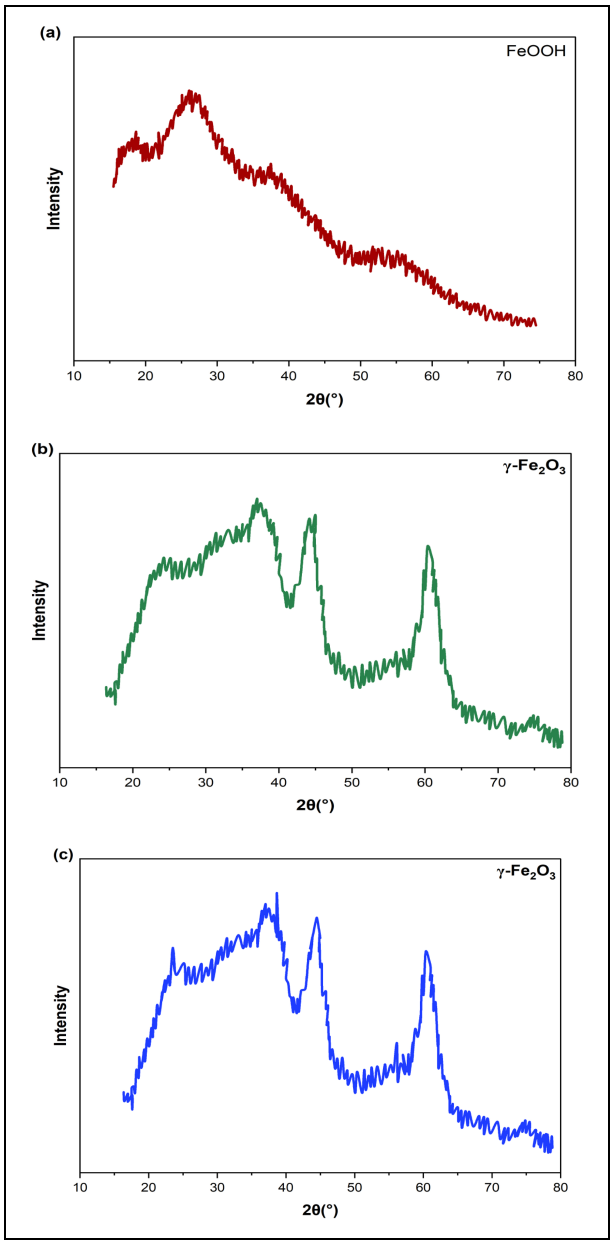


Fig. 1: XRD of FeOOH, (b) 0.15 $Fe(OH)_3$ and (c) 0.20 $Fe(OH)_3$ nano iron oxide (γ-Fe_2O_3)

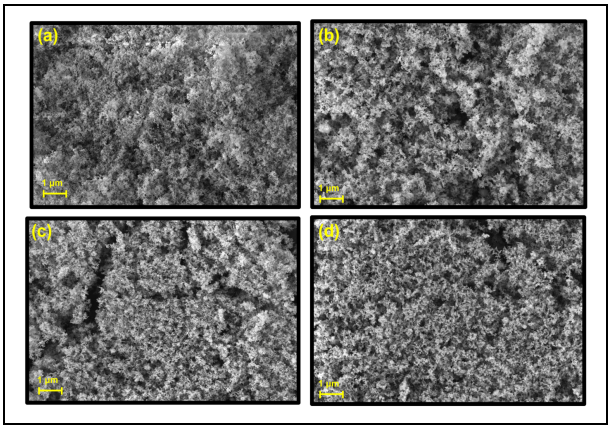


Fig. 2: SEM of (a) 0.05 (b) 0.10 (c) 0.15 and (d) 0.20 M γ-Fe_2O_3

The XRD examination confirms transformation of boehmite to γ-Fe_2O_3 during calcination at 450°C, a recognized method for producing fine γ-Fe_2O_3 from boehmite.

Thermogravimetric (TGA) and differential scanning calorimetry (DSC) analyses were performed to investigate the thermal behavior and phase evolution of the iron precursor (Reda, 2010). The TGA curve exhibits an initial weight loss below 250°C, which is attributed to the removal of physically adsorbed moisture and loosely bound hydroxyl groups. A second weight loss region observed between 300–400°C corresponds to the dehydroxylation of iron oxyhydroxide (FeOOH) and its transformation into gamma-Fe_2O_3 (maghemite). The associated endothermic peak in the DSC curve confirms this dehydration process. The range of transition temperature aligns closely with the documented transformation temperature of boehmite to iron oxide. The TGA graph in Figure 3 indicates that weight loss of boehmite happens at two distinct stages as temperature rises.

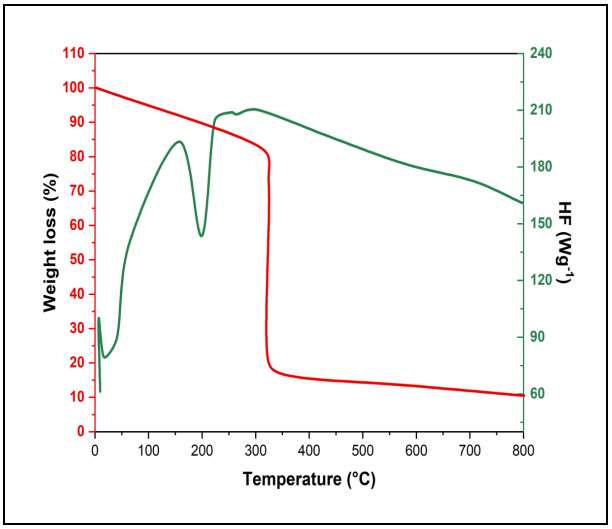


Fig. 3: TGA (red) and DSC (green) synthesized boehmite (FeOOH)

The FTIR spectra were recorded to verify existence of the Fe–O bond in the γ-Fe_2O_3 nanoparticles. The FTIR for 0.15 M $Fe(OH)_3$ - γ-Fe_2O_3, as illustrated at Figure 4, exhibit two prominent absorption areas. Absorption in the lower frequency range (1150–440 cm^{-1}) primarily pertains to Fe–O vibrations (Liu *et al.* 2018).

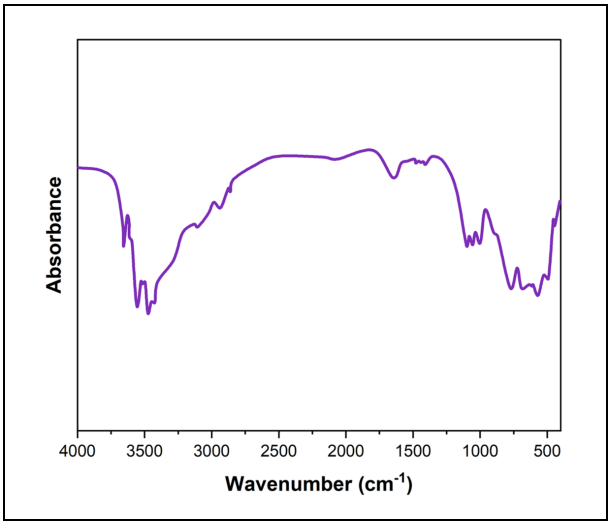


Fig. 4: FTIR 0.05 gamma nano iron oxide

The broad absorption peak observed in the high-frequency region (3650–3100 cm^{-1}) corresponds to O–H stretching vibrations of surface hydroxyl groups and adsorbed water molecules. The peak at 2943 cm^{-1} may be attributed to residual organic species or adsorbed atmospheric impurities rather than Fe–O bonding. The characteristic absorption bands at 567 and 454 cm^{-1} are assigned to Fe–O stretching vibrations associated with tetrahedral and octahedral sites of gamma-Fe_2O_3, confirming the formation of maghemite structure. The band near 779 cm^{-1} is correlated to lattice vibration modes. The oxygen ions in gamma-Fe_2O_3 form a face-centered cubic lattice, while Fe^{3+} ions occupy tetrahedral and octahedral interstitial positions. The BET analysis revealed specific surface areas of 399, 387, and 380 m^2/g for 0.05, 0.10, and 0.15 M $Fe(OH)_3$-derived γ-Fe_2O_3 nanoparticles, respectively, which significantly decreased to 290 m^2/g for 0.20 M $Fe(OH)_3$. This reduction is attributed to particle growth and increased crystallite size at higher precursor concentration.

3.2. Nitrate Removal and Adsorption Kinetics

pH is a crucial element influencing the adsorption of nitrate onto iron oxide surfaces. The trend of nitrate removal in relation to pH change, as depicted in Fig. 5, demonstrates that a pH range of 6 to 7 is optimal for maximum nitrate removal.

The results indicate that near-neutral pH promotes optimal electrostatic interaction between positively charged gamma-Fe_2O_3 surface sites and negatively charged nitrate ions. Since neutral pH is more suitable for drinking water applications, all adsorption experiments were conducted at pH 7. The maximal nitrate adsorption at equilibrium was analyzed by graphing q_e against C_e for 0.05, 0.10, 0.15, and 0.20 M $Fe(OH)_3$ generated γ-Fe_2O_3 nanoparticles (Fig. 6).

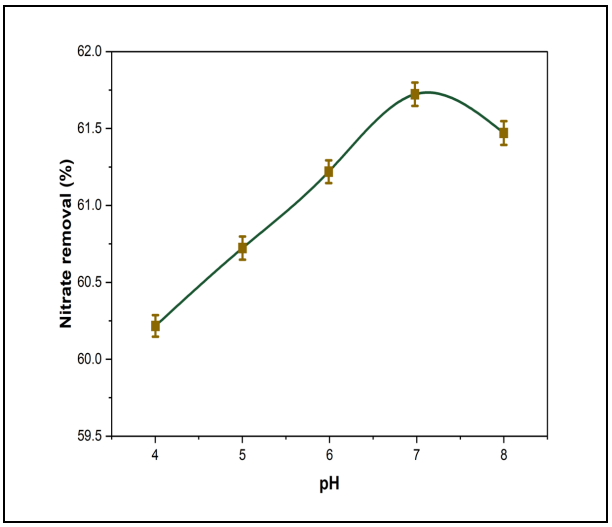


Fig. 5: Effect of pH at nitrate removal by nano- iron oxide

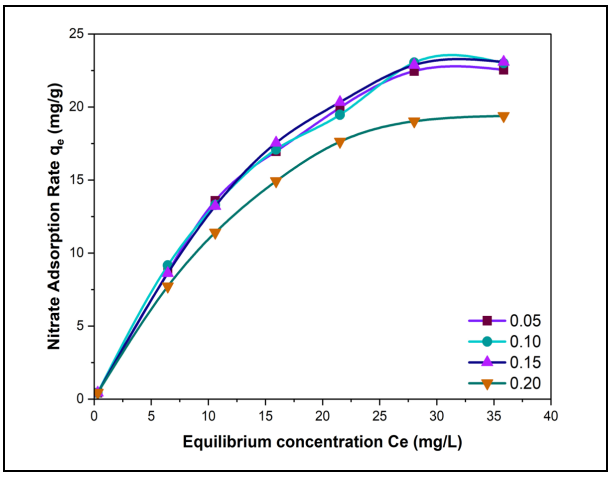


Fig. 6: Nitrate adsorption obtained for 0.05, 0.10, 0.15 and 0.20 M $Fe(OH)_3$-derived γ-Fe_2O_3 nanoparticles

The gamma-Fe_2O_3 nanoparticles synthesized at 0.05, 0.10, and 0.15 mol precursor concentrations exhibited comparable maximum adsorption capacities of 22–25 mg/g, whereas the 0.20 mol sample showed a reduced capacity of 16–19 mg/g (Biswas *et al.* 2024). The trend in nitrate removal indicates a rise in adsorption capability as the equilibrium nitrate concentration increases. The gradual increase in the isotherm indicates abundant available surface sites at low nitrate concentration, followed by progressive site saturation as concentration increases. Since 0.05, 0.10, and 0.15 M nanoparticles exhibit comparable nitrate removal capacities, detailed adsorption kinetics were conducted just for the 0.05 M $Fe(OH)_3$-derived nanoparticles. It is

noteworthy that the elevation of $Fe(OH)_3$ concentration from 0.05 to 0.15 M correspondingly augmented the yield of γ-Fe_2O_3 nanoparticles in the same proportion. Consequently, the technique refined in this study is essential for enhancing product yield.

The nitrate sorption capacity of the synthesized nanoparticles was assessed during various contact durations (Fig. 7).

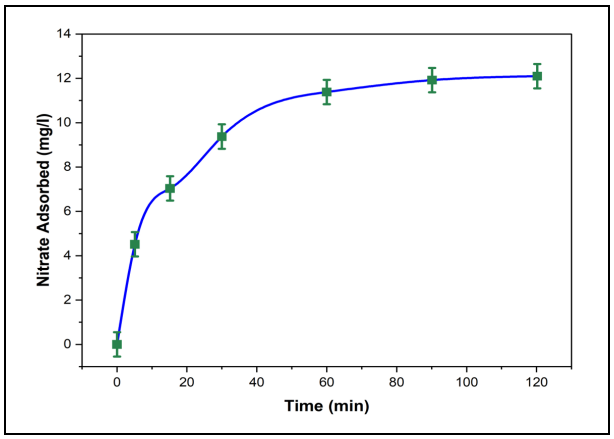


Fig. 7: Time-dependent nitrate adsorption kinetics

In the contact time experiment, 50 mg of nanoparticles were introduced 50 mL of water containing 20 mg/L of nitrate. Approximately 72% of nitrate ions were adsorbed within the first 15 minutes, after which the adsorption rate gradually decreased until equilibrium was reached. The significant nitrate adsorption seen in the initial phase is mostly attributable to the sample availability of adsorption sites on the nanoparticle surface.

The presence of competing anions like Cl^- CO_3^{2-}, NO_3^-, and SO_4^{2-}, in drinking water may affect nitrate adsorption performance of γ-Fe_2O_3 nanoparticles to a certain degree. The nitrate removal rate was assessed in the absence and presence of 50 mg/L sulfate, carbonate, chloride and nitrate anions at 50 mL of water containing 20 mg/L nitrate. The nitrate adsorption rate, depicted in the bar chart (Figure 8), demonstrates sulfate ions exert the most significant influence on nitrate adsorption, around 5.17%, followed by carbonate ions at 3.45%.

Inner-spherically adsorbing ions, such as sulfate, are observed to severely hinder nitrate adsorption. Chloride and nitrate ions was observed to exert a relatively minor influence, resulting in around a 4.31% reduction in nitrate adsorption in their presence.

3.3 Nitrate Adsorption Kinetics

Kinetics of nitrate adsorption for γ-Fe_2O_3 nanoparticles were examined by pseudo-first and second-order kinetic models. The parameters for adsorption kinetics derived from pseudo-first and second-order kinetic were given below.

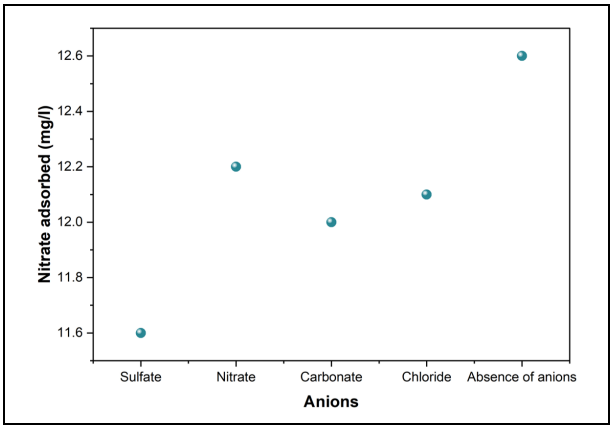


Fig. 8: Effect of chloride, carbonate, nitrate and sulfate anions on nitrate removal by gamma nanoparticles

The pseudo-first-order kinetic model is expressed as in equation (5):

$$\ln(q_e - q_t) = \ln(q_e) - k_1 t \quad \ldots (5),$$

where q_e and q_t (mg g^{-1}) are the adsorption capacities at equilibrium and at time t, respectively, and k_1 (min^{-1}) is the rate constant.

The pseudo-second-order model is denoted in equation (6):

$$t/q_t = 1/(k_2 q_e^2) + t/q_e \quad \ldots (6),$$

where k_2 (g mg^{-1} min^{-1}) is the second-order rate constant.

The results demonstrate a strong correlation between the actual and theoretical values for nitrate adsorption utilizing the γ-Fe_2O_3 nanoparticles. Fig. 9 illustrates optimal fit at pseudo-second-order, evidenced by R^2 of 0.89794.

The results align with existing research, which indicates that pseudo-second-order were observed at adsorption of nitrate ions onto iron oxide or activated iron oxide nanoparticles.

The acquired adsorption data was further evaluated utilizing the Freundlich and Langmuir models according to Equations 7 and 8.

$$1/q_e = 1/q_m + 1/bC_e q_m \quad \ldots (7)$$

$$\log(q_e) = \log(k_f) + \log(C_e) + 1/nb \ldots (8),$$

where q_e represents quantity of nitrate adsorbed on equilibrium concentration C_e represents the Langmuir constant q_m, which denotes the highest adsorption capacity; b is Langmuir constant linked with activation energy; 1/n, k_f are Freundlich constants pertaining to

adsorption intensity and capacity. Similarly in prior studies, $Fe(OH)_3$-treated Tilapia and Sciaenops fish scales removed up to 76% fluoride from drinking water. Adsorption followed pseudo-second-order kinetics and Freundlich isotherm behavior (Nkansah *et al.* 2022). Fig. 10 illustrates Freundlich and Langmuir isotherm models. Various parameters obtained from isotherms are presented at Table 2.

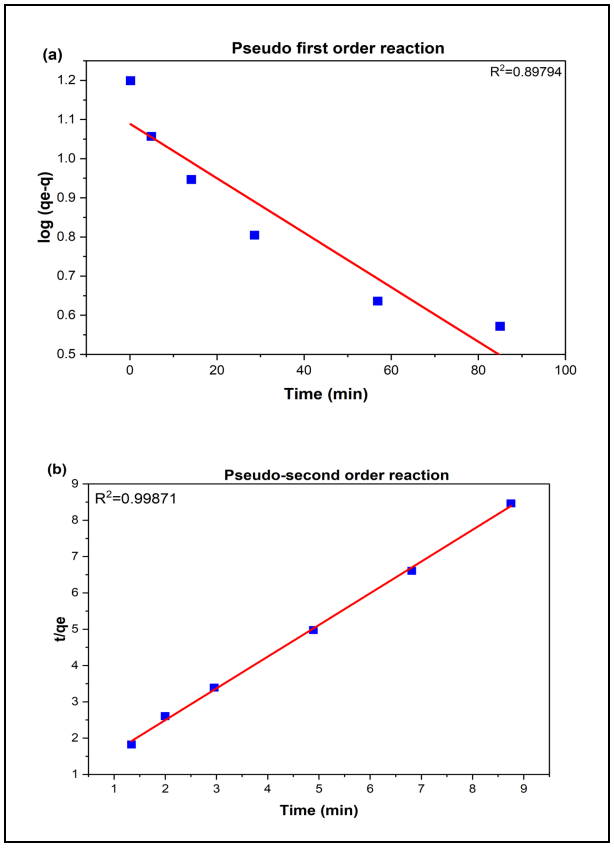


Fig. 9: (a) Pseudo-first and (b) second-order kinetic Nitrate sorption at iron oxide nanoparticles

Table 2. Parameters obtained from Freundlich and Langmuir isotherms

Freundlich constants				
1/n	K_f(mg/g)(L /mg)$^{1/n}$		R^2	
0.521	5.14		0.98383	
Langmuir constants				
q_m (exp) (mg/)	C_n (cal)	b (L/ mol)	R_2	RL
23.1	11.2	41.8	0.99197	0.27

Correlation coefficients (R^2) for Langmuir and Freundlich isotherms were determined to be 0.99197and 0.98383, respectively, indicating that Langmuir isotherm provides superior fit. The Langmuir model, which was confined to monolayer adsorption, provides current adsorption process results in the development of monolayer of nitrate adsorbate at surface of γ-Fe_2O_3 nanoparticles. The Langmuir monolayer capacity (q_m) was calculated to be approximately 25.4 mg g^{-1}, which agrees well with the experimentally observed maximum adsorption capacity (~25 mg g^{-1} for the 0.15 mol sample). The b value derived from Langmuir isotherm was subsequently employed to calculate R_L values by following equation:

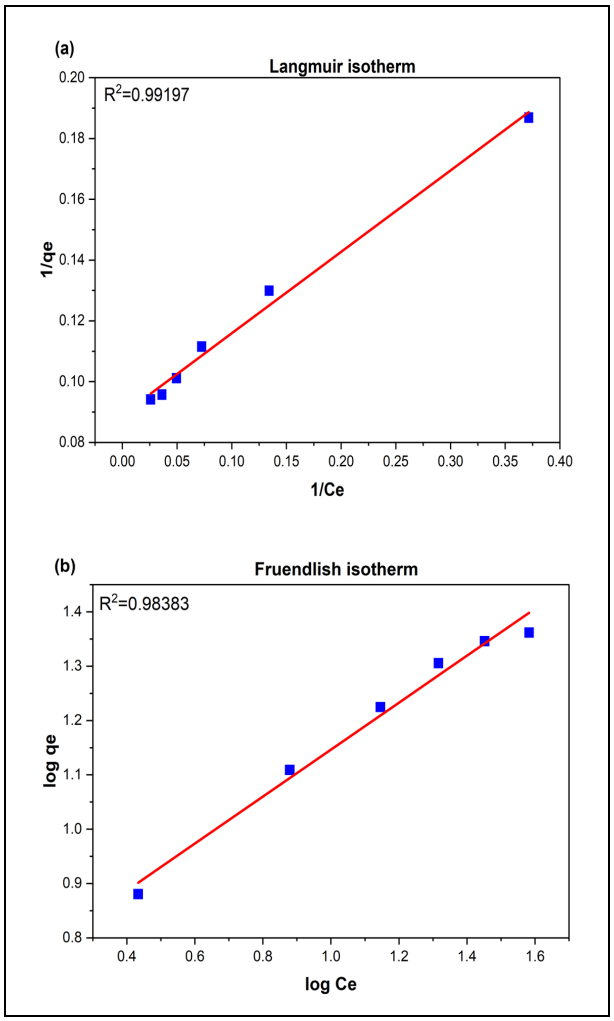


Fig. 10: (a) Langmuir and (b) Freundlich isotherm

$$R_L = 1/1 + bC_0 \quad \ldots (9)$$

The R_L value for specimen was 0.20, indicating that adsorption process utilizing γ-Fe_2O_3 nanoparticles was highly favorable. Thermodynamic feasibility of the adsorption process was assessed by computing standard free energy utilizing subsequent formula: G° = −RT ln(K), T denotes temperature in Kelvin, K signifies equilibrium constant, R represents universal gas constant (8.314 J/mol/K). The ΔG° value obtained from the

aforementioned relation was −5.2 kJ/mol, indicating a spontaneous and thermodynamically beneficial adsorption process.

The adsorption of nitrate onto iron oxide involves the electrostatic substitution of adsorbed hydroxyl ions with nitrate ions.

$$n\mathrm{Fe}^{3+}(\mathrm{aq}) + 3n - m\mathrm{OH} - (\mathrm{aq}) + m\,\mathrm{F} - (\mathrm{aq}) \rightarrow \mathrm{Fe}_n\,\mathrm{F}_m(\mathrm{OH})3n - m(\mathrm{s}) \quad \ldots (10)$$

Nitrate adsorption occurs *via* electrostatic attraction and ligand exchange at surface Fe–OH sites of γ-Fe_2O_3. At near-neutral pH, surface protonation enhances nitrate interaction through the formation of ≡Fe–OH_2^+ species. Consequently, the nitrate adsorption characterized by the two-step reaction.

$$n\mathrm{Fe}^{3+} + 3n - m\mathrm{OH} \rightarrow \mathrm{Fen}\,(\mathrm{OH})_{3n-m}(\text{ adsorption reaction }) \quad \ldots (11)$$

$$\mathrm{Fen}(\mathrm{OH})_{3n-m} + 3n - m\,\mathrm{F} \rightarrow \mathrm{Fen}(\,\mathrm{F})_{3n-m} + 3n - m\mathrm{OH} - (\text{ substitution reaction }) \quad \ldots (12)$$

At the surface of nano iron oxide particles, negatively charged hydroxide ions and positively charged iron species form $Fe_n(OH)_{3n-m}$. The nitrate ion exhibits a higher affinity for Fe^{3+}, hence competing with hydroxyl ions for replacement.

The current study unequivocally demonstrates a superior nitrate adsorption for 0.05, 0.10, and 0.15 M $Fe(OH)_3$ in comparison to 0.20 M $Fe(OH)_3$ generated gamma-$Fe2O_3$ nanoparticles. The enhanced nitrate removal rate is mostly attributed to the greater surface area of nano iron oxide particles synthesized from 0.05, 0.10, and 0.15 M $Fe(OH)_3$. The Langmuir isotherm validates surface phenomena which directly depend on surface area of nanoparticles. The reduced adsorption of nitrate by 0.20 M $Fe(OH)_3$-derived γ-Fe_2O_3 nanoparticles can be ascribed to their diminished surface area and larger particle sizes. In this study, the reaction conditions have been modified to enhance the nanoparticle yield, achieving a nitrate removal of around 25 mg/g. However, additional investigations are required to examine the impact of temperature at yield of γ-Fe_2O_3 derived from optimal molar concentrations of the $Fe(OH)_3$ precursor.

4. CONCLUSIONS

γ-Fe_2O_3 (maghemite) nanoparticles were successfully synthesized *via* a controlled precipitation–aging–calcination method using $Fe(OH)_3$ as the precursor. Structural analysis confirmed the formation of a cubic spinel γ-Fe_2O_3 phase with crystallite size increasing at higher precursor concentrations. The optimal precursor loading (0.15 mol) produced nanoparticles with high surface area and superior nitrate adsorption performance. The maximum experimentally observed nitrate adsorption capacity was approximately 25 mg g^{-1} for the optimized sample, while higher precursor concentration (0.20 mol) resulted in reduced adsorption efficiency due to crystallite growth and decreased surface area. Kinetic analysis indicated that the adsorption process followed a pseudo-second-order model, while equilibrium data were best described by the Langmuir isotherm, suggesting monolayer adsorption on homogeneous surface sites. Nitrate adsorption was governed by electrostatic interaction and surface complexation involving Fe–OH groups of γ-Fe_2O_3. Although the synthesized nanoparticles demonstrated promising adsorption capacity under controlled laboratory conditions, further studies are required to evaluate regeneration efficiency, long-term stability, and performance in real water matrices containing competing ions. Future work should focus on adsorption–desorption cycling, column studies, and testing under natural groundwater conditions to assess practical applicability. The present study establishes a clear relationship between precursor concentration, crystallite growth, and nitrate adsorption behavior, providing insight for optimizing γ-Fe_2O_3-based adsorbents for water treatment applications.

FUNDING

This research received no specific grant from any funding agency in the public, commercial, or not-for-profit sectors.

CONFLICTS OF INTEREST

The authors declare that there is no conflict of interest.

COPYRIGHT

This article is an open-access article distributed under the terms and conditions of the Creative Commons Attribution (CC BY) license (http://creativecommons.org/licenses/by/4.0/).

REFERENCES

Alagha, L., Guo, L., Ghuzi, M., Molatlhegi, O. and Xu, Z., Adsorption of hybrid polyacrylamides on anisotropic kaolinite surfaces: Effect of polymer characteristics and solution properties, *Colloids Surf. A: Physicochem. Eng. Aspects*, 498, 285–296(2016). https://doi.org/10.1016/j.colsurfa.2016.03.031

Baburao, B., Devi, K. V., Balakrishnan, V., Venkatesa Prabhu, V. P., Hariprabhu, M., Selvaraju, S., Shine, S. and Khaled, J. M., Evaluation of detoxification performance of Pithecellobium dulce seed pod powder upon acid treatment: removal of reactive red 195-A dye and kinetic analysis, *Zeitschrift Fur Physikalische Chemie*, 239(6), 885–910(2025). https://doi.org/10.1515/zpch-2024-0879

Bakr, M. M. A., Wang, Y., Hao, P., Dawoud, M. M. A., Peng, L. and Wang, Y., Biochar from Al $(OH)_3$-activated sugarcane bagasse for efficient removal of cadmium: Optimization using the response surface method (RSM), *Biomass Convers. Biorefine.*, 15(12), 19487–19504(2025). https://doi.org/10.1007/s13399-025-06594-6

Biswas, B., Parveen, N. and Goel, S., Optimization of Electrocoagulation for Natural Organic Matter Removal and Its Impact on Disinfection By-Products Formation, *J. Environ. Eng.,* 150(8), 24032(2024). https://doi.org/10.1061/JOEEDU.EEENG-7579

Demirkalp, G., Alamut, S., Arar, Ö., Yüksel, Ü. and Yüksel, M., Removal of Fluoride from water by Al (III)-loaded and Al $(OH)_3$-coated chelating resin, *Desalin. Water Treat.*, 57(34), 15910–15919(2016). https://doi.org/10.1080/19443994.2015.1074117

Dong, G., Yuan, Z., Yuan, Z. and Guo, X., Structure and functional properties of aluminum hydroxide reinforced bamboo-derived cellulose acetate composite film for biodegradable packaging, *Polym. Compos.*, 45(10), 8984–8996(2024). https://doi.org/10.1002/pc.28389

El Nahrawy, A. M., Bakr, A. M., Hemdan, B. A. and Abou Hammad, A. B., Identification of Fe^{3+} co-doped zinc titanate mesostructures using dielectric and antimicrobial activities, *Int. J. Environ. Sci. Technol.*, 17(11), 4481–4494(2020). https://doi.org/10.1007/s13762-020-02786-x

Fan, J., Liu, X., Yang, M., Liu, M., Ma, Q., Fu, L., Min, X. and Huang, Z., Synthesis of zeolite 4A from low-grade kaolin containing muscovite and quartz via ultrafast Joule heating route: A comparison with conventional calcination, *Appl. Clay Sci.*, 275, 107889(2025). https://doi.org/10.1016/j.clay.2025.107889

Girimurugan, R., Selvaraju, S., Shine, S. and Khaled, J. M., Investigation on Polypyrrole-Induced Modification of Aspergillus flavus: Evaluation of Biocompatibility and Electrochemical Properties, *J. New Mater. Electrochem. Syst.*, 27(3), 190–198(2024). https://doi.org/10.14447/jnmes.v27i3.a04

Hu, H., Yang, L., Lin, Z., Xiang, X., Jiang, X. and Hou, L., Preparation and characterization of novel magnetic Fe_3O_4/chitosan/$Al(OH)_3$ beads and its adsorption for fluoride, *Int. J. Bio. Macromol.*, 114, 256–262(2018). https://doi.org/10.1016/j.ijbiomac.2018.03.094

Kumar, A. and Basu, D., Optimization and prediction of SO_4^{2-}removal in electrocoagulation process with rotating electrodes using Taguchi and ANN approach, *J. Environ. Chem. Eng.*, 13(3), 116934(2025). https://doi.org/10.1016/j.jece.2025.116934

Liu, Y., Qian, P., Yu, Y., Yu, B., Wang, Y., Ye, S. and Chen, Y., Preparation and characterization of a novel hybrid chelating material for effective adsorption of Cu(II) and Pb(II), *J. Environ. Sci., (China)*, 67, 224–236(2018). https://doi.org/10.1016/j.jes.2017.08.026

Masindi, V., A novel technology for neutralizing acidity and attenuating toxic chemical species from acid mine drainage using cryptocrystalline magnesite tailings, *J. Water Process Eng.*, 10, 67–77(2016). https://doi.org/10.1016/j.jwpe.2016.02.002

Mayakannan, M., Prabakar, S. and Vinoth, E., Synthesis of copper sulfate supported cobalt oxide nanoparticles through microwave irradiation assisted method, *Inorg. Nano-Metal Chem.*, 53(8), 831–836(2023). https://doi.org/10.1080/24701556.2021.1977820

Nkansah, M. A., Dua, A. B., Aryee, G. A. and Adusei-Gyamfi, J., Evaluation of Scales of Tilapia Sp. and Sciaenops ocellatus as Low Cost and Green Adsorbent for fluoride Removal from Water, *Front. Chem.*, 10, 813533(2022). https://doi.org/10.3389/fchem.2022.813533

Nyangi, M. J., Chebude, Y., Kilulya, K. F. and Salim, C. J., Comparative Study on Adsorption Isotherm and Kinetics of Defluoridation Using Aluminum and Iron Electrodes in Electrocoagulation, *Chem. Africa*, 4(2), 391–398(2021). https://doi.org/10.1007/s42250-021-00228-w

Reda, S. M., Synthesis of ZnO and Fe_2O_3 nanoparticles by solgel method and their application in dye-sensitized solar cells, *Mater. Sci. Semiconduct. Proce.*, 13(5–6), 417–425(2010). https://doi.org/10.1016/j.mssp.2011.09.007

Sharma, S., Sharma, K., Acharya, S. and Khandegar, V., Feasibility and sludge analysis of electrocoagulation process for Direct Violet-35 dye remediation, *Waste Manage. Bulletin*, 2(2), 171–180(2024). https://doi.org/10.1016/j.wmb.2024.04.007

Shoppert, A., Valeev, D., Alekseev, K. and Loginova, I., Enhanced Precipitation of Gibbsite from Sodium Aluminate Solution by Adding Agglomerated Active $Al(OH)_3$ Seed, *Met.*, 13(2), (2023). https://doi.org/10.3390/met13020193

Song, M., He, J., Liu, Y., Wu, Y. and Su, Y., Degradation of tetracycline by photocatalysis combined with activated peroxymonsulfate over S-scheme $BiVO_4/Fe_2O_3$ heterojunction, *J. Environ. Chem. Eng.*, 12(5), 113300(2024). https://doi.org/10.1016/j.jece.2024.113300

Su, Y., Liu, R. and Chen, Z., Study of cadmium ion absorption using nano aluminiun hydroxide-polyacrylamide hybrid flocculation, *Lizi Jiaohuan Yu Xifu/Ion Exchange Adsorp*, 32(4), 324–332(2016). https://doi.org/10.16026/j.cnki.iea.2016040324

Tang, W., Yu, Y., Huang, Z., Wang, W., Lin, S., Luo, J., Zhang, C. and Zhang, Z., Low-Temperature Formation of Aluminum Nitride Powder from Amorphous Aluminum Oxalate via Carbothermal Reduction, *Inorg.*, 13(10), 317(2025). https://doi.org/10.3390/inorganics13100317

Tural, B., Betül Sopac, Š., Özkan, N., Demir, A. S. and Volkan, M., Preparation and characterization of surface modified γ-Fe_2O_3 (maghemite)silica nanocomposites used for the purification of benzaldehyde lyase, *J. Phy. Chem. Sol.*, 72(8), 968–973(2011). https://doi.org/10.1016/j.jpcs.2011.05.010

Wang, P., Ji, W., Wang, Y., Kou, X. and Yuan, Y., Mechanism of graphite driven electrode electrocoagulation for deep treatment of fluorine-containing wastewater, *Chinese J. Environ. Eng.*, 19(1), 135–143(2025). https://doi.org/10.12030/j.cjee.202408017

Wen, J., Yuan, R., Jiang, T., Yu, T. and Zhang, Y., Solvothermal synthesis and adsorption performance of layered boehmite using aluminum chloride and high-alumina fly ash, *Chinese J. Chem. Eng.*, 70, 280–290(2024). https://doi.org/10.1016/j.cjche.2024.03.008

Xu, K., Hao, T., Wang, H., Zheng, X., Yao, X., Li, J., Zhang, Y. and Liu, Z., Experimental and theoretical study on the hydrogen evolution inhibition performance of Herba speranskia tuberculata extract on Al alloy waste dust, *J. Environ. Chem. Eng.*, 13(1), 115262(2025a). https://doi.org/10.1016/j.jece.2024.115262

Xu, Y., Bao, W. J., Wei, F. G. and Jiang, Z. C., Probing Dynamic Interfacial Evolution in Al(OH)3-Coated $CaC0_3$ Composite Materials via Multispectral Synergy, *Guang Pu Xue Yu Guang Pu Fen Xi/Spectroscopy and Spectral Analysis*, 45(12), 3498–3507(2025b). https://doi.org/10.3964/j.issn.1000-0593(2025)12-3498-10

Zahra, Z. J. A., Jassim, L. S., Mansoor, A. S., Rasheed, R. T., Le, N. D., Abdullah, T. A., Mansoor, H. S., Azeez, H. S., Quyen, H. H., Nguyen, H. M. and Le, P. C., Preparation, characterization, and tetracycline removal from water using aluminum oxide and zinc oxide nanoparticles, *Water Practice Technol.*, 20(4), 879–895(2025). https://doi.org/10.2166/wpt.2025.051